Probing Chern number by opacity and topological phase transition by a nonlocal Chern marker

Paolo Molignini[1], Bastien Lapierre[2], R. Chitra[3], and Wei Chen[4]

[1]T.C.M. group, Cavendish Laboratory, University of Cambridge, 19 J J Thomson Avenue, Cambridge, CB3 0HE, United Kingdom

[2]Department of Physics, University of Zurich, Winterthurerstrasse 190, 8057 Zurich, Switzerland

[3]Institute for Theoretical Physics, ETH Zurich, 8093 Zurich, Switzerland

[4]Department of Physics, PUC-Rio, Rio de Janeiro 22451-900, Brazil

E-mail: `wchen@puc-rio.br`

Abstract.
    In 2D semiconductors and insulators, the Chern number of the valence band Bloch state is an important quantity that has been linked to various material properties, such as the topological order. We elaborate that the opacity of 2D materials to circularly polarized light over a wide range of frequencies, measured in units of the fine structure constant, can be used to extract a spectral function that frequency-integrates to the Chern number, offering a simple optical experiment to measure it. This method is subsequently generalized to finite temperature and locally on every lattice site by a linear response theory, which helps to extract the Chern marker that maps the Chern number to lattice sites. The long range response in our theory corresponds to a Chern correlator that acts like the internal fluctuation of the Chern marker, and is found to be enhanced in the topologically nontrivial phase. Finally, from the Fourier transform of the valence band Berry curvature, a nonlocal Chern marker is further introduced, whose decay length diverges at topological phase transitions and therefore serves as a faithful indicator of the transitions, and moreover can be interpreted as a Wannier state correlation function. The concepts discussed in this work explore multi-faceted aspects of topology and should help address the impact of system inhomogeneities.

1. Introduction

The topological order in two-dimensional (2D) time-reversal (TR) breaking systems has been an important subject in the research of topological materials, and also one of the earliest systems discovered to have nontrivial topological properties [1]. The topological invariant in these systems is described by the Chern number, which is usually detected experimentally via measuring the quantized Hall conductance [2] that in practice is attributed to the formation of edge states. The bulk band structure, on the other hand, shows the same gapped energy spectrum in both the topologically trivial and nontrivial phases, and therefore bulk measurements not involving edge states are often not considered feasible to identify the Chern number. However, the theoretical proposal

of the Chern marker and other real space constructions changed this paradigmatic viewpoint [3, 4, 5, 6, 7, 8, 9, 10, 11, 12, 13]. Through expressing the Chern number in terms of the projectors into the filled and empty bands, the Chern marker is introduced as a local quantity that is well-defined everywhere in the bulk, and recovers the Chern number in the clean, thermodynamic limit. In fact, it has been shown that such a real space formalism of topological invariant is also possible in other dimensions and symmetry classes [14, 15, 16, 17, 18, 19, 20]. It was further recognized recently that the Chern number and Chern marker are related to the circular dichroism of the 2D material [21, 22, 23, 24], and so is the Berry curvature that integrates to the Chern number [25, 26], pointing to the possibility of directly detecting the topological order by means of bulk optical measurements.

In this paper, we introduce a number of new theoretical concepts related to Chern numbers and markers and show that relatively simple opitcal experimental protocols at finite temperature can be devised to directly access bulk state topology and topological criticality. We first introduce the Chern number spectral function defined as the optical conductivity of the 2D material under circularly polarized light divided by frequency[27]. The Chern number is then given by the frequency integration of this spectral function. We then show that this can be readily detected from the opacity (measured in units of the fine structure constant) of the 2D material to circularly polarized light, as previously done in graphene[28, 29]. This experimental protocol is then generalized to individual lattice sites, leading to the conclusion that the spectral function of the Chern marker can be extracted from the absorption power under circularly polarized light on each site. Additionally, we show that its rich internal spatial structure is represented by a Chern correlator, which is nothing but the nonlocal current-current correlator. The magnitude of the correlator is found to increase as the system enters topologically nontrivial phases, suggesting that the inherent fluctuations associated with the Chern number become more dramatic in the nontrivial phases. Finally, to characterize the quantum criticality near topological phase transitions (TPTs), we introduce the nonlocal Chern marker. This is defined from the off-diagonal elements of the Chern operator, in contrast to the usual Chern marker defined from the diagonal element of the same operator. We see that this nonlocal Chern marker is equivalent to a previously proposed correlation function that measures the overlap between Wannier functions localized at different home cells [30, 31, 32], and becomes long-ranged as the system approaches TPTs, owing to the diverging Berry curvature in momentum space.

2. Linear response theory of local Chern marker

2.1. Local Chern marker in terms of Wannier states

As our work primarily explores the link between Chern markers and putative experimental measurables, we first review the original derivation of the Chern marker by Bianco and Resta [7], with an emphasis on the relation to Wannier states in the

homogeneous case. We use the following notations for the bands and Bloch states: indices n and m denote the valence and conduction bands respectively, while ℓ denotes both bands. We denote $|\ell^{\mathbf{k}}\rangle$ as the periodic part of the Bloch state, and $|\psi_{\ell\mathbf{k}}\rangle$ as the full state that is related to the former by $\langle\mathbf{r}|\psi_{\ell\mathbf{k}}\rangle = e^{i\mathbf{k}\cdot\mathbf{r}}\langle\mathbf{r}|\ell^{\mathbf{k}}\rangle$. In the homogeneous and thermodynamic limit, the Bloch state of each band $|\ell^{\mathbf{k}}\rangle$ defines a Wannier state $|\mathbf{R}\ell\rangle$ by

$$|\ell^{\mathbf{k}}\rangle = \sum_{\mathbf{R}} e^{-i\mathbf{k}\cdot(\hat{\mathbf{r}}-\mathbf{R})}|\mathbf{R}\ell\rangle, \quad |\mathbf{R}\ell\rangle = \sum_{\mathbf{k}} e^{i\mathbf{k}\cdot(\hat{\mathbf{r}}-\mathbf{R})}|\ell^{\mathbf{k}}\rangle, \tag{1}$$

where $\hat{\mathbf{r}}$ is the position operator, $\mathbf{R}$ is a Bravais lattice vector, and the normalization factors are ignored for simplicity. The Wannier function at position $\mathbf{r} = (x,y)$ is given by $\langle\mathbf{r}|\mathbf{R}n\rangle = W_n(\mathbf{r}-\mathbf{R})$, which localizes around the home cell $\mathbf{R}$ in real space.

For a general model that contains N_- valence bands, the periodic part of the fully antisymmetric valence band state at momentum $\mathbf{k}$ is given by

$$|n^{\text{val}}(\mathbf{k})\rangle = \frac{1}{\sqrt{N_-!}}\epsilon^{n_1 n_2 \ldots n_{N-}}|n_1^{\mathbf{k}}\rangle|n_2^{\mathbf{k}}\rangle\ldots|n_{N_-}^{\mathbf{k}}\rangle, \tag{2}$$

where $\epsilon^{n_1 n_2 \ldots n_{N-}}$ is the fully antisymmetric Levi-Civita symbol. The Berry curvature of this valence band state in Eq. (2) on the xy-plane of a 2D system is given by [33]

$$\Omega_{xy}(\mathbf{k}) \equiv i\langle\partial_x n^{\text{val}}|\partial_y n^{\text{val}}\rangle - i\langle\partial_y n^{\text{val}}|\partial_x n^{\text{val}}\rangle$$
$$= \sum_n \left[i\langle\partial_x n^{\mathbf{k}}|\partial_y n^{\mathbf{k}}\rangle - i\langle\partial_y n^{\mathbf{k}}|\partial_x n^{\mathbf{k}}\rangle\right], \tag{3}$$

where $\partial_\mu \equiv \partial/\partial k_\mu$. Note that the Berry curvature is additive in the curvatures of each individual valence band. We rewrite the corresponding Chern number $\mathcal{C}$ defined from the momentum integration of $\Omega_{xy}(\mathbf{k})$ as [7]

$$\mathcal{C} = \int \frac{d^2\mathbf{k}}{(2\pi)^2}\Omega_{xy}(\mathbf{k}) = \sum_{n,m}\int \frac{d^2\mathbf{k}}{(2\pi)^2}i\langle\partial_x n^{\mathbf{k}}|m^{\mathbf{k}}\rangle\langle m^{\mathbf{k}}|\partial_y n^{\mathbf{k}}\rangle - (x \leftrightarrow y). \tag{4}$$

In the following, we extensively use the identity linking the non-Abelian Berry connection to the charge polarization of the eigenstates and Wannier states [7, 34, 35, 36, 30, 31]

$$i\langle m^{\mathbf{k}}|\partial_x n^{\mathbf{k}}\rangle = \langle\psi_{m\mathbf{k}}|\hat{x}|\psi_{n\mathbf{k}}\rangle/\hbar$$
$$= \frac{1}{\hbar}\sum_{\mathbf{R}} e^{i\mathbf{k}\cdot\mathbf{R}}\langle\mathbf{0}m|\hat{x}|\mathbf{R}n\rangle = \frac{1}{\hbar}\sum_{\mathbf{R}} e^{-i\mathbf{k}\cdot\mathbf{R}}\langle\mathbf{R}m|\hat{x}|\mathbf{0}n\rangle \quad \forall\ m \neq n, \tag{5}$$

where $\hat{x}$ is the x-component of the position operator $\hat{\mathbf{r}}$ in real space. Using Eq. (5), $\mathcal{C}$ can be expressed in terms of the Wannier states [7]:

$$\mathcal{C} = \sum_{nm}\int \frac{d^2\mathbf{k}}{(2\pi)^2}\frac{i}{\hbar^2}\langle\psi_{n\mathbf{k}}|\hat{x}|\psi_{m\mathbf{k}}\rangle\langle\psi_{m\mathbf{k}}|\hat{y}|\psi_{n\mathbf{k}}\rangle - (x \leftrightarrow y)$$
$$= \frac{1}{a^2}\sum_{nm}\int \frac{d^2\mathbf{k}}{(2\pi\hbar/a)^2}\int \frac{d^2\mathbf{k}'}{(2\pi\hbar/a)^2}i\langle\psi_{n\mathbf{k}}|\hat{x}|\psi_{m\mathbf{k}'}\rangle\langle\psi_{m\mathbf{k}'}|\hat{y}|\psi_{n\mathbf{k}}\rangle - (x \leftrightarrow y)$$
$$= \frac{1}{a^2}\sum_{nm}\sum_{\mathbf{R}}i\langle\mathbf{0}n|\hat{x}|\mathbf{R}m\rangle\langle\mathbf{R}m|\hat{y}|\mathbf{0}n\rangle - (x \leftrightarrow y)$$

$$= \frac{1}{a^2} \sum_{nm} \sum_{\mathbf{R}} i \int d\mathbf{r} \int d\mathbf{r}' x_{\mathbf{r}} W_n^*(\mathbf{r}) W_m(\mathbf{r} - \mathbf{R}) y_{\mathbf{r}'} W_m^*(\mathbf{r}' - \mathbf{R}) W_n(\mathbf{r}')$$
$$- (x \leftrightarrow y), \tag{6}$$

where the second line is valid because the matrix elements for $\mathbf{k} \neq \mathbf{k}'$ vanish. In terms of the projection operators to the valence and conduction band states

$$\hat{P} = \sum_n \int \frac{d^2\mathbf{k}}{(2\pi\hbar/a)^2} |\psi_{n\mathbf{k}}\rangle\langle\psi_{n\mathbf{k}}|, \quad \hat{Q} = \sum_m \int \frac{d^2\mathbf{k}'}{(2\pi\hbar/a)^2} |\psi_{m\mathbf{k}'}\rangle\langle\psi_{m\mathbf{k}'}|, \tag{7}$$

the Chern number can be recast as

$$\mathcal{C} = \frac{i}{Na^2} \text{Tr} \left[\hat{P}\hat{x}\hat{Q}\hat{y} - \hat{P}\hat{y}\hat{Q}\hat{x} \right] = \frac{i}{Na^2} \text{Tr} \left[\hat{P}\hat{x}\hat{Q}\hat{y}\hat{P} - \hat{P}\hat{y}\hat{Q}\hat{x}\hat{P} \right], \tag{8}$$

where Tr denotes the trace over all the degrees of freedom on the lattice, and it is known that in practice an additional projector $\hat{P}$ has to be added to get the correct Chern marker locally on each site[7], as introduced below. In fact, this extra projector can also be derived from a universal topological marker constructed from spectrally flattened Dirac Hamiltonians[20]. The operator $\hat{\mathcal{C}} \equiv i[\hat{P}\hat{x}\hat{Q}\hat{y}\hat{P} - \hat{P}\hat{y}\hat{Q}\hat{x}\hat{P}]$ will be referred to as the Chern operator.

The Chern marker is introduced by considering a 2D tight-binding Hamiltonian $H = \sum_{\mathbf{rr}'\sigma\sigma'} t_{\mathbf{rr}'\sigma\sigma'} c_{\mathbf{r}\sigma}^\dagger c_{\mathbf{r}'\sigma'}$ with eigenstates satisfying $H|E_l\rangle = E_l|E_l\rangle$. In terms of $|E_l\rangle$, the projectors in Eq. (7) take the form

$$\hat{P} = \sum_n |E_n\rangle\langle E_n|, \quad \hat{Q} = \sum_m |E_m\rangle\langle E_m|. \tag{9}$$

The local Chern marker is defined by[7]

$$\mathcal{C}(\mathbf{r}) = \frac{1}{a^2} \sum_\sigma \langle \mathbf{r}, \sigma | \hat{\mathcal{C}} | \mathbf{r}, \sigma \rangle \equiv \frac{i}{a^2} \langle \mathbf{r} | \left[\hat{P}\hat{x}\hat{Q}\hat{y}\hat{P} - \hat{P}\hat{y}\hat{Q}\hat{x}\hat{P} \right] |\mathbf{r}\rangle. \tag{10}$$

In the following sections, we will present a formalism that generalizes both the Chern number $\mathcal{C}$ and the Chern marker $\mathcal{C}(\mathbf{r})$ to finite temperature, introduce their spectral functions, and suggest a simple optical measurement to detect them in contrast to traditional Hall conductance measurements.

2.2. Opacity measurement of finite temperature Chern number

The connection between the zero temperature Chern number and circular dichroism has been discussed in multiple works [21, 22, 23, 24]. Here, we discuss a finite temperature generalization of these ideas. Via the finite temperature Chern number spectral function that represents a distribution of Chern number in energy, we show that the Chern number can be simply measured from the opacity of the 2D material to circularly polarized light. We define the current operators $\hat{j}_{c1} = \hat{j}_x + i\hat{j}_y$ and $\hat{j}_{c2} = \hat{j}_x - i\hat{j}_y$ at momentum $\mathbf{k}$ where $\hat{j}_\mu(\mathbf{k}) = e\partial_\mu H(\mathbf{k})$ with e the electron charge and $H(\mathbf{k})$ the unperturbed single-particle Hamiltonian. These currents are relevant to the two circularly polarized oscillating electric fields $\mathbf{E}^{c1}(t) = (\hat{\mathbf{x}} + i\hat{\mathbf{y}})E_0 e^{-i\omega t}$ and $\mathbf{E}^{c2}(t) = (\hat{\mathbf{x}} - i\hat{\mathbf{y}})E_0 e^{-i\omega t}$. Due to minimal coupling $\delta H = -\mathbf{j} \cdot \mathbf{A}$ and $\mathbf{E} = -\partial\mathbf{A}/\partial t$,

the two polarizations induce the corresponding perturbations: $\delta H^{c1}(\mathbf{k}) = \hat{j}_{c1} i E_0 e^{-i\omega t}/\omega$ and $\delta H^{c2}(\mathbf{k}) = \hat{j}_{c2} i E_0 e^{-i\omega t}/\omega$. Within linear response theory, the polarization induced currents satisfy $\langle \hat{j}_{c2} \rangle = \sigma_{c2,c1}(\mathbf{k}, \omega) E_0 e^{-i\omega t}$ and $\langle \hat{j}_{c1} \rangle = \sigma_{c1,c2}(\mathbf{k}, \omega) E_0 e^{-i\omega t}$, where the optical conductivity σ is

$$\sigma_{c1,c2}(\mathbf{k}, \omega) = \sum_{\ell < \ell'} \frac{\pi}{a^2 \hbar \omega} \langle \ell | \hat{j}_{c1} | \ell' \rangle \langle \ell' | \hat{j}_{c2} | \ell \rangle$$

$$\times \left[f(\varepsilon_\ell^{\mathbf{k}}) - f(\varepsilon_{\ell'}^{\mathbf{k}}) \right] \delta(\omega + \frac{\varepsilon_\ell^{\mathbf{k}}}{\hbar} - \frac{\varepsilon_{\ell'}^{\mathbf{k}}}{\hbar}), \tag{11}$$

Note, $\sigma_{c2,c1}(\mathbf{k}, \omega)$ is given by the same expression with $\hat{j}_{c1} \leftrightarrow \hat{j}_{c2}$. Here $|\ell\rangle \equiv |\ell^{\mathbf{k}}\rangle$ is the periodic part of the Block state, and the index ℓ enumerates both the valence and conduction band states, since at finite temperature both of them contribute to the Chern number, and $f(\varepsilon_\ell^{\mathbf{k}})$ is the Fermi distribution of the eigenenergy $\varepsilon_\ell^{\mathbf{k}}$. Note that the δ-function in Eq. (11) with $\omega > 0$ ensures $\varepsilon_\ell^{\mathbf{k}} < \varepsilon_{\ell'}^{\mathbf{k}}$, such that it only accounts for the optical absorption process, as denoted by the notation $\sum_{\ell < \ell'}$. To proceed, we introduce the Berry curvature spectral function at momentum $\mathbf{k}$ by

$$\Omega_{xy}^d(\mathbf{k}, \omega) = \sum_{\ell < \ell'} \left[i \langle \partial_x \ell | \ell' \rangle \langle \ell' | \partial_y \ell \rangle - (x \leftrightarrow y) \right]$$

$$\times \left[f(\varepsilon_\ell^{\mathbf{k}}) - f(\varepsilon_{\ell'}^{\mathbf{k}}) \right] \delta(\omega + \frac{\varepsilon_\ell^{\mathbf{k}}}{\hbar} - \frac{\varepsilon_{\ell'}^{\mathbf{k}}}{\hbar}), \tag{12}$$

which has been derived from a linear response theory[26]. When integrated over frequency, this function recovers the Berry curvature in Eq. (3) in the zero temperature limit where $\ell \to n$ and $\ell \to m$. Using Eq. (11) and $\langle \ell | \hat{j}_\mu | \ell' \rangle = e \left(\varepsilon_\ell^{\mathbf{k}} - \varepsilon_{\ell'}^{\mathbf{k}} \right) \langle \partial_\mu \ell | \ell' \rangle$, we find the following relation

$$\sigma_{c2,c1}(\mathbf{k}, \omega) - \sigma_{c1,c2}(\mathbf{k}, \omega) = 2 \frac{\pi e^2}{a^2} \hbar \omega \, \Omega_{xy}^d(\mathbf{k}, \omega). \tag{13}$$

Further integration over momentum [27]

$$\sigma_{c2,c1}(\omega) - \sigma_{c1,c2}(\omega) = \int \frac{d^2 \mathbf{k}}{(2\pi\hbar/a)^2} \left[\sigma_{c2,c1}(\mathbf{k}, \omega) - \sigma_{c1,c2}(\mathbf{k}, \omega) \right]$$

$$= \frac{2\pi e^2}{\hbar} \omega \int \frac{d^2 \mathbf{k}}{(2\pi)^2} \Omega_{xy}^d(\mathbf{k}, \omega) \equiv \frac{2\pi e^2}{\hbar} \omega \, \mathcal{C}^d(\omega), \tag{14}$$

defines what we call the Chern number spectral function $\mathcal{C}^d(\omega)$. Physically, $\mathcal{C}^d(\omega)$ can be interpreted as a "density of states" of the Chern number $\mathcal{C}^d$ indicating which eigenstates contribute the most to the Chern number, as we shall see in the following sections using concrete examples. In our notation, the superscript d stands for "dressed" to indicate that it is a finite temperature generalization of the Chern number.

To relate the spectral function in Eq. (14) to experimental observables, we write the real part of the circularly polarized oscillating fields and the currents they induce as

$$\mathbf{E}^{c1}(\omega, t) = E_0(\hat{\mathbf{x}} + i\hat{\mathbf{y}}) \cos \omega t,$$

$$\mathbf{j}_{c2}(\omega, t) = \sigma_{c2,c1}(\omega) \mathbf{E}^{c1*}(\omega, t) = \sigma_{c2,c1}(\omega) E_0(\hat{\mathbf{x}} - i\hat{\mathbf{y}}) \cos \omega t,$$

$$\mathbf{E}^{c2}(\omega, t) = E_0(\hat{\mathbf{x}} - i\hat{\mathbf{y}}) \cos \omega t,$$

$$\mathbf{j}_{c1}(\omega, t) = \sigma_{c1,c2}(\omega) \mathbf{E}^{c2*}(\omega, t) = \sigma_{c1,c2}(\omega) E_0(\hat{\mathbf{x}} + i\hat{\mathbf{y}}) \cos \omega t, \tag{15}$$

where E_0 is the strength of the field. The absorption power at each circular polarization is then given by

$$W_a^{c1}(\omega) = \langle \mathbf{j}^{c2}(\omega, t) \cdot \mathbf{E}^{c1}(\omega, t) \rangle_t = \sigma_{c2,c1}(\omega) E_0^2,$$
$$W_a^{c2}(\omega) = \langle \mathbf{j}^{c1}(\omega, t) \cdot \mathbf{E}^{c2}(\omega, t) \rangle_t = \sigma_{c1,c2}(\omega) E_0^2, \tag{16}$$

where the time average gives $\langle \cos^2 \omega t \rangle_t = 1/2$. On the other hand, the incident power of the light per unit cell area of each polarization is $W_i = c\varepsilon_0 E_0^2 |\hat{\mathbf{x}} \pm i\hat{\mathbf{y}}|^2/2 = c\varepsilon_0 E_0^2$, so the difference in opacity for the two polarizations is $\mathcal{O}^{c1}(\omega) - \mathcal{O}^{c2}(\omega) = [W_a^{c1}(\omega) - W_a^{c2}(\omega)]/W_i$, which can be used to extract the Chern number spectral function and subsequently the Chern number by

$$\mathcal{C}^d(\omega) = \frac{1}{8\pi\omega}\left[\frac{\mathcal{O}^{c1}(\omega) - \mathcal{O}^{c2}(\omega)}{\pi\alpha}\right], \quad \mathcal{C}^d = \int_0^\infty d\omega\, \mathcal{C}^d(\omega), \tag{17}$$

where $\alpha = e^2/4\pi c\varepsilon_0 \hbar$ is the fine structure constant[28]. In other words, the Chern number spectral function can be simply extracted from the opacity difference between the two circular polarizations, similar to measurements in graphene[28, 29]. Moreover, because the finite temperature Chern number $\mathcal{C}^d$ is the frequency integrated spectral function, Eq. (17) implies that the opacity difference under circularly polarized light divided by frequency and then integrated over frequency must be a quantized integer at zero temperature, thereby realizing a topology induced frequency sum rule for noninteracting 2D materials [27]. This simple experimental protocol is easily accessible, thereby permitting a direct verification of the concepts proposed in our work.

2.3. Linear response theory of finite temperature Chern marker

The finite temperature Chern number can further be written into real space using the formalism in Sec. 2.1, yielding

$$\begin{aligned}
\mathcal{C}^d &= \frac{a^2}{\hbar^2} \int \frac{d^2\mathbf{k}}{(2\pi\hbar/a)^2} \sum_{\ell < \ell'} [i\langle \partial_x \ell | \ell' \rangle \langle \ell' | \partial_y \ell \rangle - (x \leftrightarrow y)] \left[f(\varepsilon_\ell^\mathbf{k}) - f(\varepsilon_{\ell'}^\mathbf{k})\right] \\
&= \frac{1}{a^2} \int \frac{d^2\mathbf{k}}{(2\pi\hbar/a)^2} \sum_{\ell < \ell'} \left[i\langle \psi_\ell^\mathbf{k} | \hat{x} | \psi_{\ell'}^\mathbf{k} \rangle \langle \psi_{\ell'}^\mathbf{k} | \hat{y} | \psi_\ell^\mathbf{k} \rangle - (x \leftrightarrow y)\right] \left[f(\varepsilon_\ell^\mathbf{k}) - f(\varepsilon_{\ell'}^\mathbf{k})\right] \\
&= \frac{1}{a^2} \int \frac{d^2\mathbf{k}}{(2\pi\hbar/a)^2} \int \frac{d^2\mathbf{k}'}{(2\pi\hbar/a)^2} \\
&\quad \sum_{\ell < \ell'} \left[i\langle \psi_\ell^\mathbf{k} | \hat{x} | \psi_{\ell'}^{\mathbf{k}'} \rangle \langle \psi_{\ell'}^{\mathbf{k}'} | \hat{y} | \psi_\ell^\mathbf{k} \rangle - (x \leftrightarrow y)\right] \left[f(\varepsilon_\ell^\mathbf{k}) - f(\varepsilon_{\ell'}^{\mathbf{k}'})\right] \\
&= \frac{1}{Na^2} \sum_{\ell < \ell'} [i\langle E_\ell | \hat{x} | E_{\ell'} \rangle \langle E_{\ell'} | \hat{y} | E_\ell \rangle - (x \leftrightarrow y)] [f(E_\ell) - f(E_{\ell'})] \\
&= \frac{1}{Na^2} \sum_{\ell < \ell'} \mathrm{Tr}\left[i\hat{x} S_{\ell'} \hat{y} S_\ell - (x \leftrightarrow y)\right] [f(E_\ell) - f(E_{\ell'})], \tag{18}
\end{aligned}$$

where $|E_\ell\rangle$ is a lattice eigenstate obtained from diagonalizing the lattice Hamiltonian $H|E_\ell\rangle = E_\ell |E_\ell\rangle$, and we denote its projector by $S_\ell = |E_\ell\rangle\langle E_\ell|$. Here $|\psi_\ell^\mathbf{k}\rangle$ is the full

Bloch state satisfying $\langle \mathbf{r}|\psi_\ell^\mathbf{k}\rangle = e^{i\mathbf{k}\cdot\mathbf{r}}\langle \mathbf{r}|\ell\rangle$, and in deriving Eq. (18) we have used

$$\int \frac{d^2\mathbf{k}}{(2\pi\hbar/a)^2}|\psi_\ell^\mathbf{k}\rangle\langle\psi_\ell^\mathbf{k}| = \sum_\ell S_\ell,$$

$$\int \frac{d^2\mathbf{k}}{(2\pi\hbar/a)^2}|\psi_\ell^\mathbf{k}\rangle\langle\psi_\ell^\mathbf{k}|f(\varepsilon_\ell^\mathbf{k}) = \sum_\ell S_\ell f(E_\ell), \tag{19}$$

At zero temperature, the Fermi distribution becomes a step function hence the indices $\ell \to n$ and $\ell' \to m$ are limited to the valence and conduction bands, respectively, so the Chern number in Eq. (18) recovers the zero temperature results in Eqs. (6) and (8).

However, from the discussion after Eq. (8), an extra projector analogous to P must be added to Eq. (18) in order to obtain the right Chern marker. The issue is then how should one consistently add a projector given that the thermal broadening at finite temperature renders the filled and empty states projectors P and Q in Eq. (7) rather ambiguous. For this purpose, we propose to first evaluate the matrix

$$X = \sum_{\ell<\ell'} S_\ell \hat{x} S_{\ell'} \sqrt{f_{\ell\ell'}}, \tag{20}$$

and the analogous Y given by replacing $\hat{x} \to \hat{y}$, where $f_{\ell\ell'} \equiv f(E_\ell) - f(E_{\ell'})$. Having calculated these matrices, we define the finite temperature Chern marker by

$$\mathcal{C}^d(\mathbf{r}) = \frac{i}{a^2}\langle\mathbf{r}|\left[X\,Y^\dagger - Y\,X^\dagger\right]|\mathbf{r}\rangle, \tag{21}$$

i.e., it is the diagonal element of the operator $i[X\,Y^\dagger - Y\,X^\dagger]$ that serves as the finite temperature generalization of the Chern operator defined after Eq. (8). The legitimacy of Eq. (21) relies on the fact that it encapsulates proper thermal broadening and spatially sums to the Chern number $\mathcal{C}^d = \sum_\mathbf{r}\mathcal{C}^d(\mathbf{r})/N$ in Eq. (18) since $\sum_\mathbf{r}|\mathbf{r}\rangle\langle\mathbf{r}| = I$ and $S_\ell S_{\bar\ell} = S_\ell\delta_{\ell\bar\ell}$. Essentially, our proposal is based on the assertion that the $\hat{P}\hat{x}\hat{Q}$ factor in Eq. (8) is generalized to the X operator in Eq. (20) at finite temperature in order to be consistent with our linear response theory of optical conductivity, i.e., the spatial sum of the Chern marker is proportional to the global Hall conductance.

Extending Eq. 20 to the frequency-dependent matrix

$$X(\omega) = \sum_{\ell<\ell'} S_\ell \hat{x} S_{\ell'} \sqrt{f_{\ell\ell'}}\,\delta(\omega + E_\ell/\hbar - E_{\ell'}/\hbar), \tag{22}$$

(and the analogous $Y(\omega)$), a generalized Chern marker spectral function can now be extracted:

$$\mathcal{C}^d(\mathbf{r},\omega) = \mathrm{Re}\left[\frac{i}{a^2}\langle\mathbf{r}|\left[X(\omega)Y^\dagger(\omega) - Y(\omega)X^\dagger(\omega)\right]|\mathbf{r}\rangle\right]. \tag{23}$$

It is straightforward to see that $\mathcal{C}^d(\omega) = \sum_\mathbf{r}\mathcal{C}^d(\mathbf{r},\omega)/N$ (cf. Eq. (14)). Based on Sec. 2.2 we immediately conclude that the Chern marker spectral function represents the local opacity difference at the unit cell at $\mathbf{r}$:

$$\mathcal{C}^d(\mathbf{r},\omega) = \frac{1}{8\pi\omega}\left[\frac{\mathcal{O}^{c1}(\mathbf{r},\omega) - \mathcal{O}^{c2}(\mathbf{r},\omega)}{\pi\alpha}\right], \quad \mathcal{C}^d(\mathbf{r}) = \int_0^\infty d\omega\,\mathcal{C}^d(\mathbf{r},\omega). \tag{24}$$

The local opacity sums to the global one $\mathcal{O}^{c1}(\omega) = \sum_{\mathbf{r}} \mathcal{O}^{c1}(\mathbf{r}, \omega)$. As a result, $\mathcal{C}^d(\mathbf{r}, \omega)$ in principle can be detected by performing the opacity measurement described after Eq. (17) locally at $\mathbf{r}$. However, at zero temperature, one should keep in mind that $\mathcal{C}^d(\mathbf{r}, \omega)$ is nonzero only at frequencies larger than the band gap of the material $\omega > \Delta$. Typical semiconducting band gaps $\Delta \sim$ eV likely necessitate circularly polarized light in the visible light range. As the wave lengths far exceed the lattice constant in this range, it will hinder the detection of local opacity in the nanometer scale. Nevertheless, we anticipate that $\mathcal{C}^d(\mathbf{r}, \omega)$ may be detected by thermal probes such as scanning thermal microscopy[37, 38, 39, 40] that can detect the heating at the atomic scale caused by the circularly polarized light. The detected local absorption power $W_a^{c1}(\mathbf{r}, \omega) - W_a^{c2}(\mathbf{r}, \omega)$ then leads to Eq. (24) as a heating rate of the unit cell at $\mathbf{r}$.

3. Lattice model of Chern insulator

We now illustrate the power of the concepts described in the previous sections by exploring the concrete example of a prototypical 2D Chern insulator. The momentum space Hamiltonian in the basis $(c_{\mathbf{k}s}, \; c_{\mathbf{k}p})^T$ is given by [41, 42]

$$
\begin{aligned}
H(\mathbf{k}) = {} & 2t \sin k_x \sigma^x + 2t \sin k_y \sigma^y \\
& + \left(M + 4t' - 2t' \cos k_x - 2t' \cos k_y \right) \sigma^z.
\end{aligned}
\tag{25}
$$

The internal degrees of freedom $\sigma = \{s, p\}$ are the orbitals. A straightforward Fourier transform leads to the two band lattice Hamiltonian [43]

$$
\begin{aligned}
H = {} & \sum_i t \left\{ -i c_{is}^\dagger c_{i+ap} + i c_{i+as}^\dagger c_{ip} - c_{is}^\dagger c_{i+bp} + c_{i+bs}^\dagger c_{ip} + h.c. \right\} \\
& + \sum_{i\delta} t' \left\{ -c_{is}^\dagger c_{i+\delta s} + c_{ip}^\dagger c_{i+\delta p} + h.c. \right\} \\
& + \sum_i (M + 4t') \left\{ c_{is}^\dagger c_{is} - c_{ip}^\dagger c_{ip} \right\},
\end{aligned}
\tag{26}
$$

where $\delta = \{a, b\}$ represents the lattice constants in the two planar directions. Throughout the paper, we set $t = t' = 1.0$ and tune the mass term M to examine different topological phases, and the behavior of this model at finite temperature T. The model hosts topological phase transitions (TPT) at three critical points $M_c = \{-8, -4, 0\}$, reflecting gap closures at different high symmetry points (HSPs) in momentum space [44]. Since they all exhibit the same critical behavior [30, 31, 32], we will focus on the $M_c = 0$ critical point where the bulk gap closes at $\mathbf{k} = (0, 0)$.

Analytical results for this model can be obtained by linearizing the Hamiltonian near the HSP $\mathbf{k}_0 = (0, 0)$, yielding $E_{m,n} = \pm\sqrt{M^2 + v^2 k^2}$ and a zero temperature Berry curvature $\Omega_{xy} = v^2 M / 2 \left(M^2 + v^2 k^2 \right)^{3/2}$. The finite temperature Chern number spectral function in Eq. (14) is given by

$$
\mathcal{C}^d(\omega) = \frac{M}{2\pi\hbar\omega^2} \left[f\left(-\frac{\hbar\omega}{2} \right) - f\left(\frac{\hbar\omega}{2} \right) \right]_{\omega \geq 2|M|/\hbar}.
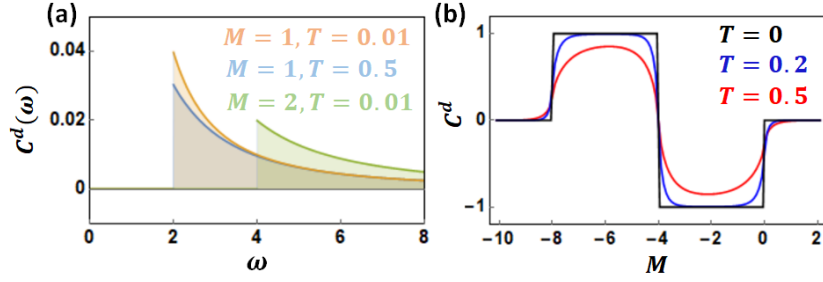\tag{27}
$$

Figure 1. (a) The Chern number spectral function $\mathcal{C}^d(\omega)$ for the Chern insulator in a continuum, which is finite only at frequency larger than the bulk gap M, and moreover scales like $1/\omega^2$ such that it integrates to a topological invariant. The overall magnitude reduces with temperature. (b) The frequency-integrated Chern number $\mathcal{C}^d$ at zero and nonzero temperatures as a function of the mass term M.

At $T = 0$, $\mathcal{C}^d(\omega) \rightarrow \mathcal{C}(\omega)$ and is nonzero only if $\omega \geq 2|M|/\hbar$, since it represents an exciton absorption rate, as shown schematically in Fig. 1 (a). Moreover, the topological invariant $\mathcal{C} = \int_{2|M|/\hbar}^{\infty} d\omega \, \mathcal{C}(\omega) = \text{Sgn}(M)/4\pi$. Essentially, this is the f-sum rule for exciton absorption rates in circular dichroism applied to topological insulators [27]. When $T \neq 0$, since the Fermi factor $f\left(-\frac{\omega}{2}\right) - f\left(\frac{\omega}{2}\right) \leq 1$, $\mathcal{C}^d < \text{Sgn}(M)/4\pi$ smaller than the true topological invariant, as illustrated in Fig. 1 (a). We anticipate that these predicted features should be readily verifiable by the opacity experiment proposed in Secs. 2.2.
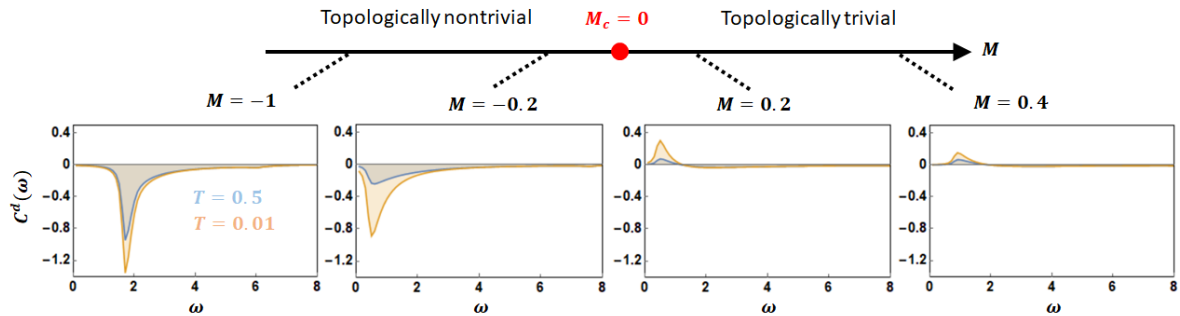

Figure 2. The Chern number spectral function $\mathcal{C}^d(\omega)$ for the lattice model of Chern insulator as a function of $M = \{-1, -0.2, 0.2, 0.4\}$ across the critical point $M_c = 0$, plotted for both low (orange) and high (blue) temperatures, where the δ-function in Eq. (27) is simulated by a Lorentzian with width $\eta = 0.1$. In the topologically nontrivial phase $M = \{-1, -0.2\}$, the spectral function is negative due to the negative Chern number $\mathcal{C}^d \approx -1$, and the spectral weight gradually shifts to low frequency as $M \rightarrow M_c$. In the topologically trivial phase $M = \{0.2, 0.4\}$ and at low temperature, the positive and negative regions together yield $\mathcal{C}^d \approx 0$ (up to numerical precision).

The numerical results of the Chern number/marker $\mathcal{C}^d = \mathcal{C}^d(\mathbf{r})$ for the homogeneous lattice model of Chern insulator in Eq. (25) are shown in Fig. 1 (b). One sees that though the abrupt changes of the Chern number at the critical points are smeared out at nonzero

temperature, clear vestiges of these TPTs are still present and should be observable in the experimentally accessible temperature range. To explain this smearing and examine the critical behavior, in Fig. 2 we present the evolution of the Chern number/marker spectral function $\mathcal{C}^d(\omega) = \mathcal{C}^d(\mathbf{r}, \omega)$ across the critical point M_c at both low and high temperatures. In the topologically nontrivial phase $M < 0$, the spectral function is negative (consistent with $\mathcal{C} = -1$) and the magnitude is largest near the band gap $\omega \approx 2|M|$, reflecting that excitations of states in the vicinity of the band gap are the most detrimental to the topological properties of the system. The role of temperature is to reduce the overall magnitude of the spectral function and subsequently the frequency integration, consistent with the smearing presented in Fig. 1 (b). On the other hand, in the topologically trivial phase $M > 0$, the spectral weight has both positive and negative components such that it integrates to a zero Chern number $\mathcal{C}^d \approx 0$ at low temperature. Interestingly, the effect of temperature is to reduce the positive peak at low frequency and make the overall frequency integration slightly negative, which explains the smearing of the sharp jump of $\mathcal{C}^d$ at the critical point by temperature as shown in Fig. 1 (b). Comparing the $M = -0.2$ and $M = 0.2$ panels in Fig. 2, we see that the spectral weight near the band gap flips sign as the system crosses the TPT at $M_c = 0$, in accordance with the flipping of Berry curvature at the HSP $\mathbf{k}_0 = (0,0)$, a defining feature of TPTs [45, 30, 31, 32]. This is also true at the other TPTs at $M = \{-8, -4\}$ at which $\mathcal{C}$ changes abruptly, and we anticipate that it should be readily detectable by the opacity measurement proposed in Sec. 2.2.

4. Topological quantum criticality

The Chern marker is known to display interesting critical behavior near TPTs, such as size-dependent smoothening of its discontinuity [46], Kibble-Zurek scaling in disordered Chern insulators [47], and Hofstadter-butterfly-like features in quasicrystals [48]. As with standard symmetry breaking critical points, where correlation functions of the order parameter show divergent correlation lengths, here, using linear response theory, we explore if there exist certain nonlocal correlators that will display such singular behavior near TPTs. We identify two quantities: a *Chern correlator* and a *nonlocal Chern marker*, which encode different physics pertaining to the topological quantum criticality.

4.1. Chern correlator

Based on the linear response theory presented earlier, we define a Chern correlator spectral function by splitting the second position operator $\hat{x} = \sum_{\mathbf{r}'} \hat{x}_{\mathbf{r}'}$ in Eq. (23) into its component on each site $\mathbf{r}'$, yielding

$$\tilde{\mathcal{C}}(\mathbf{r}, \mathbf{r}', \omega) = \mathrm{Re}\left[\frac{i}{a^2} \langle \mathbf{r} | \left[X(\omega) Y_{\mathbf{r}'}^\dagger(\omega) - Y(\omega) X_{\mathbf{r}'}^\dagger(\omega) \right] |\mathbf{r}\rangle \right],$$

$$X_{\mathbf{r}'}^\dagger(\omega) = \sum_{\ell < \ell'} S_{\ell'} \hat{x}_{\mathbf{r}'} S_\ell \sqrt{f_{\ell\ell'}} \delta(\omega + E_\ell/\hbar - E_{\ell'}/\hbar), \tag{28}$$

which spatially sums to the Chern marker spectra function $\mathcal{C}^d(\mathbf{r}, \omega) = \sum_{\mathbf{r}'} \tilde{\mathcal{C}}(\mathbf{r}, \mathbf{r}', \omega)$ in Eq. (23). This splitting of the second position operator is justified by the observation that in Eqs. (11) and (18), the second position operator accounts for the global field. Consequently, this Chern correlator spectral function $\tilde{\mathcal{C}}(\mathbf{r}, \mathbf{r}', \omega)$ represents the local current at site $\mathbf{r}$ caused by applying a field of frequency ω at site $\mathbf{r}'$, i.e., the nonlocal current response. A frequency integration $\tilde{\mathcal{C}}(\mathbf{r}, \mathbf{r}') = \int_0^\infty d\omega\, \tilde{\mathcal{C}}(\mathbf{r}, \mathbf{r}', \omega)$ further leads to a Chern correlator

$$\tilde{\mathcal{C}}(\mathbf{r}, \mathbf{r}') = \mathrm{Re}\left[\frac{i}{a^2} \langle \mathbf{r} | \left[X\, Y_{\mathbf{r}'}^\dagger - Y\, X_{\mathbf{r}'}^\dagger \right] | \mathbf{r} \rangle \right],$$
$$X_{\mathbf{r}'}^\dagger(\omega) = \sum_{\ell < \ell'} S_{\ell'} \hat{x}_{\mathbf{r}'} S_\ell \sqrt{f_{\ell\ell'}} \tag{29}$$

This correlator sums to the Chern marker $\sum_{\mathbf{r}'} \tilde{\mathcal{C}}(\mathbf{r}, \mathbf{r}') = \mathcal{C}^d(\mathbf{r})$ and represents a measure of the internal fluctuation of the Chern marker. Note that in a clean and infinite system, the local Chern marker $\mathcal{C}^d(\mathbf{r}) = \mathcal{C}^d$ is homogenous even in the vicinity of a TPT. However, the Chern correlator $\tilde{\mathcal{C}}(\mathbf{r}, \mathbf{r}')$ depends on $\mathbf{r} - \mathbf{r}'$ as clearly evidenced by the numerical results for the Chern insulator shown in Fig. 3.
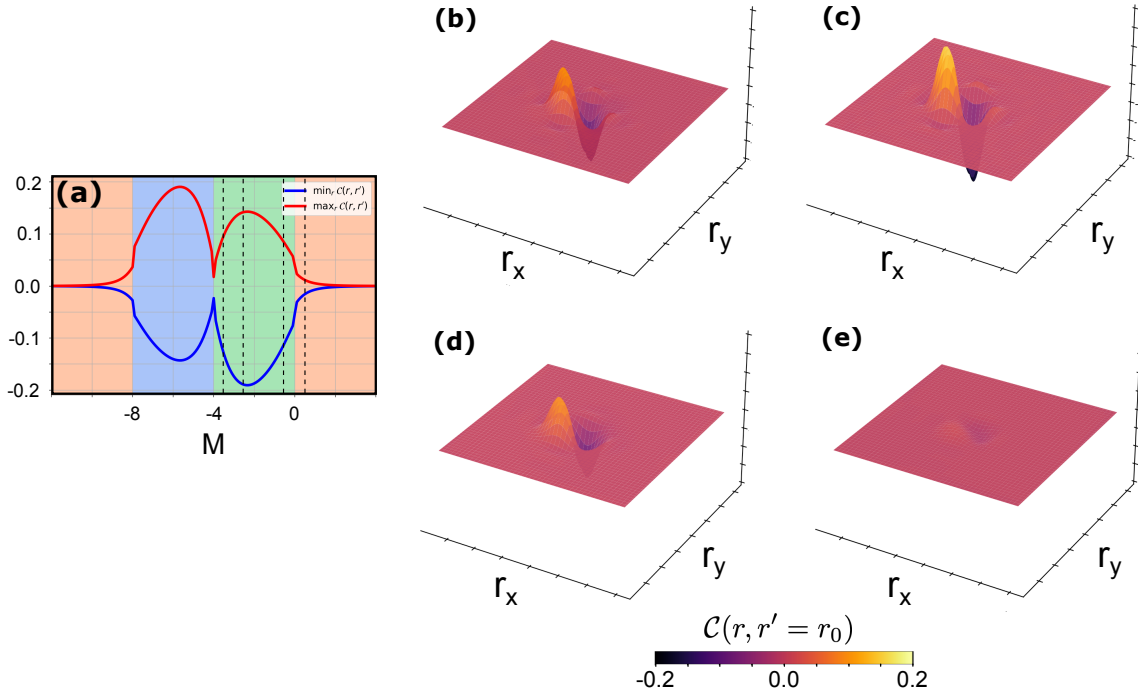

Figure 3. (a) The maximal and minimal values of the zero-temperature Chern correlator $\tilde{\mathcal{C}}(\mathbf{r}, \mathbf{r}')$ as a function of the tuning parameter M for a Chern insulator on a 14×14 lattice. The background color indicates the three topologically distinct phases. The vertical dashed lines indicate the surface plots of $\tilde{\mathcal{C}}(\mathbf{r}, \mathbf{r}' = \mathbf{r_0})$ with $r_0 = (7, 7)$, shown in the right panels: (b) $M = -3.5$, (c) $M = -2.5$, (d) $M = -0.5$, (e) $M = 0.5$. The surface plots have been interpolated on a 140×140 grid as a visual aid.

Typically, the correlations are maximal deep in a topological phase and very weak in topologically trivial phases, indicating a much larger internal fluctuation of the Chern

marker in the nontrivial phase. The Chern correlator consists mainly of two peaks of opposite sign around $\mathbf{r} \sim \mathbf{r}'$ consistent with the expectation that the nonlocal current-current correlator is larger at short separations. A pronounced asymmetry between the heights of the two peaks is seen in topologically non trivial phases whereas the peak heights are equal in the topologically trivial phase, concomitant with the expectation that the spatial integral of this correlator should yield the Chern number. These aspects are well encapsulated in Fig. 3(a) where we see the evolution of the two peak heights as a function of M. Finally, the frequency dependence of the Chern correlator spectral function $\tilde{\mathcal{C}}(\mathbf{r}, \mathbf{r}', \omega)$ is shown in Fig. 4, indicating a spatial pattern that changes dramatically with ω. Physically, this reflects the variation of the current at $\mathbf{r}$ stemming from optical absorption due to the light applied at $\mathbf{r}'$.
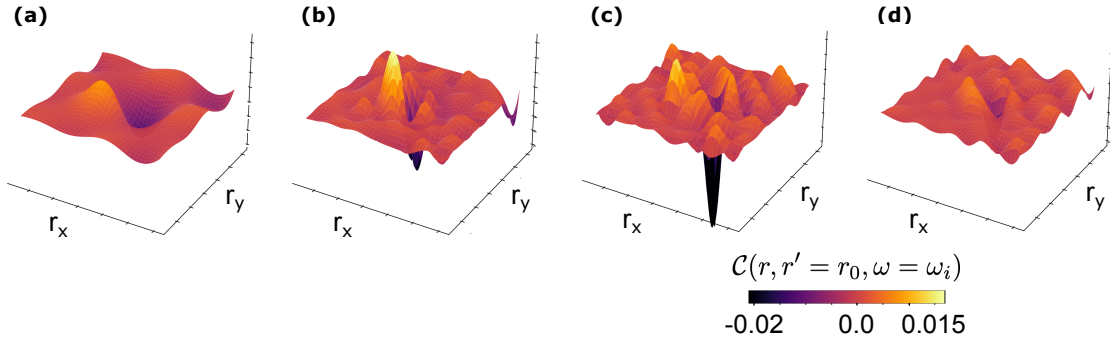

Figure 4. Chern correlator spectral function $\tilde{\mathcal{C}}(\mathbf{r}, \mathbf{r}' = r_0, \omega = \omega_i)$ at various values of the frequency ω_i for a Chern insulator at $M = -1.0$ and temperature $k_B T = 0.1$ on a 12×12 lattice. The reference point is $r_0 = (6, 6)$. (a) $\omega_i = 2.7$, (b) $\omega_i = 5.6$, (c) $\omega_i = 5.9$, (d) $\omega_i = 6.9$. In the numerics, the delta function was approximated by a Lorentzian with width parameter $\eta = 0.1$. The surface plots have been interpolated on a 120×120 grid as a visual aid.

4.2. Wannier state correlation function as a nonlocal Chern marker

Lastly, we highlight the intricate link between Chern markers and a previously proposed Wannier state correlation function [30, 31, 32]. Restricting ourselves to a homogeneous system at zero temperature, the Wannier state correlation function derived from the Fourier transform of the Berry curvature Ω_{xy} is [35, 36, 49]

$$\tilde{F}(\mathbf{R}) = \int \frac{d^2\mathbf{k}}{(2\pi)^2} \Omega_{xy}(\mathbf{k}) e^{i\mathbf{k}\cdot\mathbf{R}} = -i \sum_n \langle \mathbf{R}n|(R_x \hat{y} - R_y \hat{x})|\mathbf{0}n\rangle$$

$$= -i \sum_n \int d^2\mathbf{r}(R_x y - R_y x) W_n(\mathbf{r} - \mathbf{R})^* W_n(\mathbf{r}) \tag{30}$$

provided $\mathbf{R} \neq \mathbf{0}$. The Lorentzian shape of the Berry curvature $\Omega_{xy}(\mathbf{k})$ with width ξ^{-1} results in a decaying $\tilde{F}(\mathbf{R})$ with correlation length ξ. The spatial profile of $\tilde{F}(\mathbf{R})$ for the lattice Chern insulator of Eq. (26) is discussed in Fig. 3 of Ref. [30]. As the system approaches the TPTs, $\xi \to \infty$. This is a generic feature of TPTs both in and out of equilibirum [50, 51], from which the critical exponent of ξ can be extracted [30, 31, 32].

Using the formalism in Sec. 2.1, we also note that

$$\tilde{F}(\mathbf{R}) = \sum_n \int \frac{d^2\mathbf{k}}{(2\pi)^2} i\langle \partial_x n^{\mathbf{k}} | \partial_y n^{\mathbf{k}} \rangle e^{i\mathbf{k}\cdot\mathbf{R}} - (x \leftrightarrow y)$$

$$= \sum_n \sum_m \int \frac{d^2\mathbf{k}}{(2\pi)^2} \int \frac{d^2\mathbf{k}'}{(2\pi)^2} i\langle \psi_{n\mathbf{k}} | \hat{x} | \psi_{m\mathbf{k}'} \rangle \langle \psi_{m\mathbf{k}'} | \hat{y} | \psi_{n\mathbf{k}} \rangle e^{i\mathbf{k}\cdot\mathbf{R}}$$

$$- (x \leftrightarrow y). \tag{31}$$

Since $\mathbf{R}$ is a Bravais lattice vector and $n^{\mathbf{k}}(\mathbf{r}) = n^{\mathbf{k}}(\mathbf{r}+\mathbf{R})$ is cell periodic,

$$\langle \mathbf{r} | \psi_{n\mathbf{k}} \rangle e^{i\mathbf{k}\cdot\mathbf{R}} = e^{i\mathbf{k}\cdot(\mathbf{r}+\mathbf{R})} n^{\mathbf{k}}(\mathbf{r}+\mathbf{R}) = \psi_{n\mathbf{k}}(\mathbf{r}+\mathbf{R}) = \langle \mathbf{r}+\mathbf{R} | \psi_{n\mathbf{k}} \rangle. \tag{32}$$

In parallel, using the projector operator formalism, we can define a nonlocal Chern marker $\mathcal{C}(\mathbf{r}+\mathbf{R},\mathbf{r})$ from the off-diagonal element of the Chern operator

$$\mathcal{C}(\mathbf{r}+\mathbf{R},\mathbf{r}) \equiv \mathrm{Re}\left[\frac{i}{a^2} \langle \mathbf{r}+\mathbf{R}| \left[\hat{P}\hat{x}\hat{Q}\hat{y}\hat{P} - \hat{P}\hat{y}\hat{Q}\hat{x}\hat{P} \right] | \mathbf{r} \rangle \right]. \tag{33}$$

Note that the case $\mathbf{R} = 0$ reduces to the standard Chern marker $\mathcal{C}(\mathbf{r})$. Using Eq. (32), one sees that for homogeneous systems in the thermodynamic limit, the nonlocal Chern marker is precisely the $\tilde{F}(\mathbf{R})$

$$\lim_{N\to\infty} \mathcal{C}(\mathbf{r}+\mathbf{R},\mathbf{r}) = \tilde{F}(\mathbf{R}). \tag{34}$$

This remarkable correspondence offers a highly practical method to evaluate the Wannier state correlation function $\tilde{F}(\mathbf{R})$ in lattice models. The spatial profile of $\mathcal{C}(\mathbf{r}+\mathbf{R},\mathbf{r})$ for the lattice Chern insulator in Eq. (26) for parameters close and far away from the critical point $M_c = 0$ is shown in Fig. 5. As expected, $\mathcal{C}(\mathbf{r}+0,\mathbf{r}) = \mathcal{C}(\mathbf{r}) \approx 0$ or -1 in the two distinct topological phases and $\mathcal{C}(\mathbf{r}+\mathbf{R},\mathbf{r})$ decreases with $\mathbf{R}$. Due to the diverging correlation length ξ, $\mathcal{C}(\mathbf{r}+\mathbf{R},\mathbf{r})$ becomes more long-ranged as the system approaches the critical point $M_c = 0$ from either side of the transition, thereby serving as a faithful measure to the critical behavior near TPTs. We remark that the critical exponent of the correlation length $\xi \sim |M|^{-\nu}$ has been calculated previously from the divergence of Berry curvature, yielding $\nu = 1$ for linear Dirac models [30, 52, 32, 31, 51, 50]. Similar critical exponents can also be extracted from the scaling of the Chern marker itself [46] These features remain true for all the three critical points $M_c = \{0, -4, -8\}$ in the lattice model of Chern insulators, so we only present the data near the critical point $M_c = 0$ for simplicity. Though $\mathcal{C}(\mathbf{r}+\mathbf{R},\mathbf{r})$ does not have a straightforward interpretation within linear response theory, it can nevertheless, be extracted from Fourier transforms of the Berry curvature measured in momentum space. Importantly, as the decay length ξ is entirely determined by the Lorentzian shape of the Berry curvature at HSPs [30, 32], it suffices to probe a very small region near the HSPs to extract the decay of the Wannier correlation. Such measurements should be feasible with pump-probe experiments in 2D materials[53, 26].
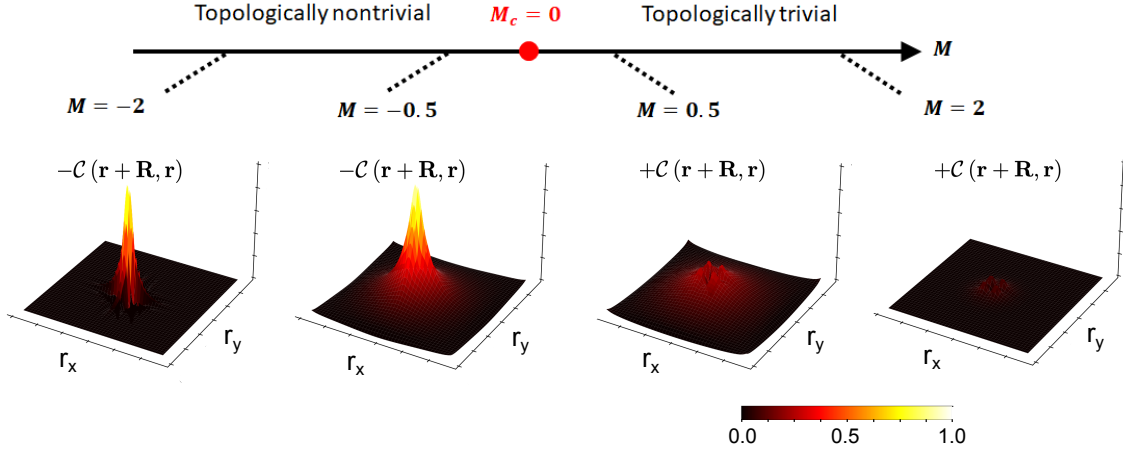
Figure 5. The nonlocal Chern marker $\mathcal{C}(\mathbf{r} + \mathbf{R}, \mathbf{r})$ of the lattice Chern insulator of size 28×28 sites, where we choose $\mathbf{r}$ to be at the center of the lattice and plot it as a function of $\mathbf{R}$ for four values of M. One sees that the spatial profiles closer to the critical point $M = \pm 0.5$ are more long-ranged than those far away from the critical point $M = \pm 2$. Note that we plot $-\mathcal{C}(\mathbf{r} + \mathbf{R}, \mathbf{r})$ for the topologically nontrivial phase since the Chern marker $\mathcal{C}(r) \approx -1$ gives an overall negative amplitude.
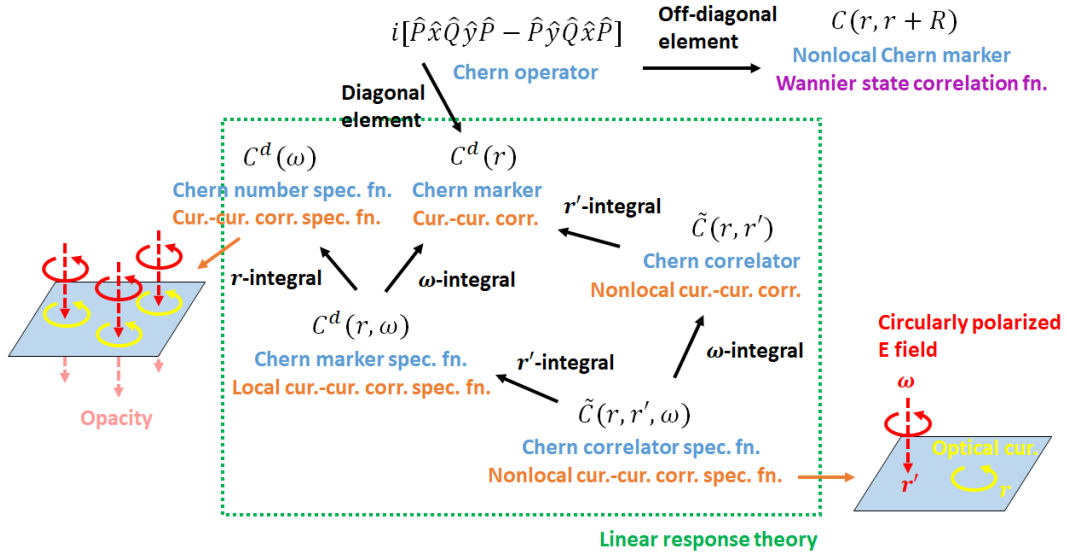

Figure 6. Summary of the linear response theory, measurement protocols, and Wannier function interpretation of various quantities introduced in the present work. The blue text gives the terminology, the orange text the corresponding physical quantity in the optical Hall response, and the black arrows the relation between them. The abbreviations are cur.-cur. corr. = current-current correlator, spec. = spectral, and fn. = function.

5. Conclusions

In summary, we unveil a number of new aspects related to the measurement of the Chern number and the identification of TPTs in 2D TR breaking materials as summarized

schematically in Fig. 6. We first identify a Chern number spectral function $\mathcal{C}^d(\omega)$ that can be extracted from the opacity of 2D materials against circularly polarized light. As the Chern number $\mathcal{C}^d$ is simply given by the frequency integration of this spectral function, our results provide a very simple experimental protocol to access bulk topology that is expected to be widely applicable to 2D materials. Generalizing the above measurement protocol to finite temperatures, we show that temperature adversely affects the low frequency part of $\mathcal{C}^d(\omega)$ thereby smearing the sharp jumps of the Chern number at zero temperature TPTs. We then propose a finite temperature Chern marker spectral function $\mathcal{C}^d(\mathbf{r}, \omega)$ which frequency-integrates to the finite temperature Chern marker. This spectral function can be measured by atomic scale thermal probes as the local heating rate caused by circularly polarized light.

To quantify critical behavior near TPTs in 2D TR breaking materials, we introduced the Chern correlator $\tilde{\mathcal{C}}(\mathbf{r}, \mathbf{r}')$ and its associated spectral function $\tilde{\mathcal{C}}(\mathbf{r}, \mathbf{r}', \omega)$. These are intimately linked to nonlocal current-current correlations in the optical Hall response. These quantities manifest different behaviours in topologically trivial and non-trivial phases. We also showed that the nonlocal Chern marker becomes increasingly long-ranged as TPTs are approached. Finally, we remark that the notions introduced in the present work have been recently generalized to TR symmetric 2D systems like the Bernevig-Hughes-Zhang model[54]described by spin Chern numbers and markers [55]. We anticipate that these new aspects may be widely applied to investigate the influence of real space inhomogeneities on both bulk topology and the critical behavior near TPTs.

6. Acknowledgments

[1] F. D. M. Haldane. Model for a quantum hall effect without landau levels: Condensed-matter realization of the "parity anomaly". *Phys. Rev. Lett.*, 61:2015–2018, October 1988.

[2] D. J. Thouless, M. Kohmoto, M. P. Nightingale, and M. den Nijs. Quantized hall conductance in a two-dimensional periodic potential. *Phys. Rev. Lett.*, 49:405–408, August 1982.

[3] J. Bellissard, A. van Elst, and H. Schulz- Baldes. The noncommutative geometry of the quantum hall effect. *J. Math. Phys.*, 35(10):5373–5451, 1994.

[4] Emil Prodan, Taylor L. Hughes, and B. Andrei Bernevig. Entanglement spectrum of a disordered topological chern insulator. *Phys. Rev. Lett.*, 105:115501, Sep 2010.

[5] Emil Prodan. Non-commutative tools for topological insulators. *New J. Phys.*, 12(6):065003, jun 2010.

[6] Emil Prodan. Disordered topological insulators: a non-commutative geometry perspective. *J. Phys. A: Math. Theor.*, 44(11):113001, feb 2011.

[7] Raffaello Bianco and Raffaele Resta. Mapping topological order in coordinate space. *Phys. Rev. B*, 84:241106, December 2011.

[8] Raffaello Bianco and Raffaele Resta. Orbital magnetization as a local property. *Phys. Rev. Lett.*, 110:087202, Feb 2013.

[9] Antimo Marrazzo and Raffaele Resta. Locality of the anomalous hall conductivity. *Phys. Rev. B*, 95:121114, Mar 2017.

[10] Alexei Kitaev. Anyons in an exactly solved model and beyond. *Ann. Phys.*, 321(1):2–111, 2006. January Special Issue.

[11] Yi-Fu Zhang, Yun-You Yang, Yan Ju, Li Sheng, Rui Shen, Dong-Ning Sheng, and Ding-Yu Xing. Coupling-matrix approach to the chern number calculation in disordered systems. *Chin. Phys. B*, 22(11):117312, nov 2013.

[12] D. Carvalho, N. A. García-Martínez, J. L. Lado, and J. Fernández-Rossier. Real-space mapping of topological invariants using artificial neural networks. *Phys. Rev. B*, 97:115453, Mar 2018.

[13] Peru d'Ornellas, Ryan Barnett, and Derek K. K. Lee. Quantized bulk conductivity as a local chern marker. *Phys. Rev. B*, 106:155124, Oct 2022.

[14] T. A. Loring and M. B. Hastings. Disordered topological insulators via c*-algebras. *EPL*, 92(6):67004, dec 2010.

[15] Ian Mondragon-Shem, Taylor L. Hughes, Juntao Song, and Emil Prodan. Topological criticality in the chiral-symmetric aiii class at strong disorder. *Phys. Rev. Lett.*, 113:046802, Jul 2014.

[16] Huaqing Huang and Feng Liu. Quantum spin hall effect and spin bott index in a quasicrystal lattice. *Phys. Rev. Lett.*, 121:126401, Sep 2018.

[17] Juntao Song and Emil Prodan. Aiii and bdi topological systems at strong disorder. *Phys. Rev. B*, 89:224203, Jun 2014.

[18] Juntao Song, Carolyn Fine, and Emil Prodan. Effect of strong disorder on three-dimensional chiral topological insulators: Phase diagrams, maps of the bulk invariant, and existence of topological extended bulk states. *Phys. Rev. B*, 90:184201, Nov 2014.

[19] Fei Song, Shunyu Yao, and Zhong Wang. Non-hermitian topological invariants in real space. *Phys. Rev. Lett.*, 123:246801, Dec 2019.

[20] Wei Chen. Universal topological marker. *Phys. Rev. B*, 107:045111, Jan 2023.

[21] Duc Thanh Tran, Alexandre Dauphin, Adolfo G. Grushin, Peter Zoller, and Nathan Goldman. Probing topology by "heating": Quantized circular dichroism in ultracold atoms. *Sci. Adv.*, 3(8):e1701207, 2017.

[22] Luca Asteria, Duc Thanh Tran, Tomoki Ozawa, Matthias Tarnowski, Benno S. Rem, Nick Fläschner, Klaus Sengstock, Nathan Goldman, and Christof Weitenberg. Measuring quantized circular dichroism in ultracold topological matter. *Nat. Phys.*, 15:449, 2019.

[23] Quentin Marsal, Dániel Varjas, and Adolfo G. Grushin. Topological weaire–thorpe models of amorphous matter. *Proceedings of the National Academy of Sciences*, 117(48):30260–30265, 2020.

[24] Philipp W. Klein, Adolfo G. Grushin, and Karyn Le Hur. Interacting stochastic topology and mott transition from light response. *Phys. Rev. B*, 103:035114, 2021.

[25] C. Repellin and N. Goldman. Detecting fractional chern insulators through circular dichroism. *Phys. Rev. Lett.*, 122:166801, Apr 2019.

[26] Wei Chen and Gero von Gersdorff. Measurement of interaction-dressed berry curvature and quantum metric in solids by optical absorption. *SciPost Phys. Core*, 5:040, 2022.

[27] Ivo Souza and David Vanderbilt. Dichroic f-sum rule and the orbital magnetization of crystals. *Phys. Rev. B*, 77:054438, February 2008.

[28] R. R. Nair, P. Blake, A. N. Grigorenko, K. S. Novoselov, T. J. Booth, T. Stauber, N. M. R. Peres, and A. K. Geim. Fine structure constant defines visual transparency of graphene. *Science*, 320(5881):1308–1308, 2008.

[29] Z. Q. Li, E. A. Henriksen, Z. Jiang, Z. Hao, M. C. Martin, P. Kim, H. L. Stormer, and D. N. Basov. Dirac charge dynamics in graphene by infrared spectroscopy. *Nat. Phys.*, 4(7):532–535, Jul 2008.

[30] Wei Chen, Markus Legner, Andreas Rüegg, and Manfred Sigrist. Correlation length, universality

classes, and scaling laws associated with topological phase transitions. *Phys. Rev. B*, 95:075116, Feb 2017.

[31] Wei Chen and Manfred Sigrist. *Advanced Topological Insulators, Ch. 7.* Wiley-Scrivener, March 2019.

[32] Wei Chen and Andreas P Schnyder. Universality classes of topological phase transitions with higher-order band crossing. *New J. Phys.*, 21(7):073003, jul 2019.

[33] Gero von Gersdorff and Wei Chen. Measurement of topological order based on metric-curvature correspondence. *Phys. Rev. B*, 104:195133, Nov 2021.

[34] Nicola Marzari and David Vanderbilt. Maximally localized generalized wannier functions for composite energy bands. *Phys. Rev. B*, 56:12847–12865, November 1997.

[35] Nicola Marzari, Arash A. Mostofi, Jonathan R. Yates, Ivo Souza, and David Vanderbilt. Maximally localized wannier functions: Theory and applications. *Rev. Mod. Phys.*, 84:1419–1475, October 2012.

[36] M. Gradhand, D. V. Fedorov, F. Pientka, P. Zahn, I. Mertig, and B. L. Györffy. First-principle calculations of the berry curvature of bloch states for charge and spin transport of electrons. *J. Phys. Condens. Matter*, 24(21):213202, 2012.

[37] A. Majumdar. Scanning thermal microscopy. *Annu. Rev. Mater. Sci.*, 29(1):505–585, 1999.

[38] Achim Kittel, Wolfgang Müller-Hirsch, Jürgen Parisi, Svend-Age Biehs, Daniel Reddig, and Martin Holthaus. Near-field heat transfer in a scanning thermal microscope. *Phys. Rev. Lett.*, 95:224301, Nov 2005.

[39] Séverine Gomès, Ali Assy, and Pierre-Olivier Chapuis. Scanning thermal microscopy: A review. *Phys. Status Solidi (a)*, 212(3):477–494, 2015.

[40] Yun Zhang, Wenkai Zhu, Fei Hui, Mario Lanza, Theodorian Borca-Tasciuc, and Miguel Muñoz Rojo. A review on principles and applications of scanning thermal microscopy (sthm). *Adv. Funct. Mater.*, 30(18):1900892, 2020.

[41] Xiao-Liang Qi and Shou-Cheng Zhang. Topological insulators and superconductors. *Rev. Mod. Phys.*, 83:1057–1110, October 2011.

[42] B. Andrei Bernevig and Taylor L. Hughes. *Topological Insulators and Topological Superconductors*. Princeton University Press, April 2013.

[43] Wei Chen. Absence of equilibrium edge currents in theoretical models of topological insulators. *Phys. Rev. B*, 101:195120, May 2020.

[44] Paolo Molignini, Antonio Zegarra, Evert van Nieuwenburg, R. Chitra, and Wei Chen. A supervised learning algorithm for interacting topological insulators based on local curvature. *SciPost Phys.*, 11:073, 2021.

[45] Wei Chen. Scaling theory of topological phase transitions. *J. Phys. Condens. Matter*, 28(5):055601, 2016.

[46] M. D. Caio, G. Möller, N. R. Cooper, and M. J. Bhaseen. Topological marker currents in chern insulators. *Nat. Phys.*, 15(3):257–261, Mar 2019.

[47] Lara Ulčakar, Jernej Mravlje, and Tomaž Rejec. Kibble-zurek behavior in disordered chern insulators. *Phys. Rev. Lett.*, 125:216601, Nov 2020.

[48] Duc-Thanh Tran, Alexandre Dauphin, Nathan Goldman, and Pierre Gaspard. Topological hofstadter insulators in a two-dimensional quasicrystal. *Phys. Rev. B*, 91:085125, Feb 2015.

[49] Xinjie Wang, Jonathan R. Yates, Ivo Souza, and David Vanderbilt. *Ab initio* calculation of the anomalous hall conductivity by wannier interpolation. *Phys. Rev. B*, 74:195118, November 2006.

[50] Paolo Molignini, Wei Chen, and R. Chitra. Generating quantum multicriticality in topological insulators by periodic driving. *Phys. Rev. B*, 101:165106, Apr 2020.

[51] P. Molignini, W. Chen, and R. Chitra. Unifying topological phase transitions in noninteracting, interacting, and periodically driven systems. *Europhys. Lett.*, 128:36001, 2019.

[52] Paolo Molignini, Wei Chen, and R. Chitra. Universal quantum criticality in static and floquet-majorana chains. *Phys. Rev. B*, 98:125129, Sep 2018.

[53] Isabella Gierz, Jesse C. Petersen, Matteo Mitrano, Cephise Cacho, I. C. Edmond Turcu, Emma

Springate, Alexander Stöhr, Axel Köhler, Ulrich Starke, and Andrea Cavalleri. Snapshots of non-equilibrium dirac carrier distributions in graphene. *Nat. Mater.*, 12(12):1119–1124, Dec 2013.

[54] B. Andrei Bernevig, Taylor L. Hughes, and Shou-Cheng Zhang. Quantum spin hall effect and topological phase transition in hgte quantum wells. *Science*, 314(5806):1757–1761, 2006.

[55] Wei Chen. Optical absorption measurement of spin berry curvature and spin chern marker. *J. Phys.: Condens. Matter*, 35(15):155601, feb 2023.